Geophysical Research Letters

RESEARCH LETTER
10.1029/2023GL107113

Investigating Convective Processes Underlying ENSO: New Insights Into the Fixed Anvil Temperature Hypothesis

Hanii Takahashi[1], Zhengzhao Johnny Luo[2], Hirohiko Masunaga[3], Rachel Storer[1,4], and Akira T. Noda[5]

[1]Jet Propulsion Laboratory, California Institute of Technology, Pasadena, CA, USA, [2]Department of Earth and Atmospheric Sciences, the City College of New York of City University of New York, New York, NY, USA, [3]Institute for Space-Earth Environmental Research, Nagoya University, Nagoya, Japan, [4]Joint Institute for Regional Earth System Science and Engineering, University of California, Los Angeles, CA, USA, [5]Japan Agency for Marine-Earth Science and Technology, Yokohama, Japan

Key Points:

- LNB is lower during El Niño due to a greater UT stability, but convective outflow levels remain consistent across ENSO cycles
- The intensity of convective cores during El Niño has to be stronger than that during La Niña
- Our finding necessitates a modification to FAT and the proportionately higher anvil temperature (PHAT)

Correspondence to:

H. Takahashi,
Hanii.Takahashi@jpl.nasa.gov

Citation:

Takahashi, H., Luo, Z. J., Masunaga, H., Storer, R., & Noda, A. T. (2024). Investigating convective processes underlying ENSO: New insights into the fixed anvil temperature hypothesis. *Geophysical Research Letters*, *51*, e2023GL107113. https://doi.org/10.1029/2023GL107113

Received 1 NOV 2023
Accepted 4 MAR 2024

Author Contributions:

Conceptualization: Hanii Takahashi, Zhengzhao Johnny Luo, Hirohiko Masunaga, Akira T. Noda
Formal analysis: Zhengzhao Johnny Luo
Investigation: Hanii Takahashi, Zhengzhao Johnny Luo, Hirohiko Masunaga, Rachel Storer
Methodology: Hanii Takahashi, Zhengzhao Johnny Luo, Hirohiko Masunaga
Supervision: Hanii Takahashi, Zhengzhao Johnny Luo
Validation: Hanii Takahashi, Zhengzhao Johnny Luo, Hirohiko Masunaga, Rachel Storer
Visualization: Hanii Takahashi

Abstract Interannual variations provide insight into the sensitivity of convective processes. Thus, CloudSat and ERA5 are used to explore the relationship among convective cores, outflows and environmental conditions during El Niño-Southern Oscillation (ENSO) cycles. Results reveal greater upper-tropospheric stability during El Niño, resulting in a lower level of neutral buoyancy compared to La Niña. However, outflow levels remain relatively consistent across ENSO cycles. This suggests that, despite less favorable conditions for deep convection during El Niño, stronger convective intensity is required to achieve outflow levels comparable to those in La Niña. Indeed, our results suggest that convection observed during El Niño tends to have broader cores and lower entrainment rates, translating to greater intensity compared to La Niña. These findings emphasize the importance of considering both large-scale and convective-scale processes, providing an update to the fixed anvil temperature (FAT) and the proportionately higher anvil temperature (PHAT) hypotheses as originally proposed.

Plain Language Summary Examining year-to-year variations provides unique insights into understanding how storms may change in a warmer climate. We use CloudSat and ERA5 reanalysis to examine variations in convective outflow (i.e., an airflow pushed out of storms), environmental factors, and cloud properties during ENSO cycles. Comparing El Niño to La Niña, we find that the atmosphere higher up in the troposphere tends to be more stable, which usually slows down the development of storms, during El Niño. However, the heights where convective outflow occurs do not change much during El Niño and La Niña events. This happens because during El Niño, the upward movement of air in storms is more powerful. This stronger upward movement offsets the stabilizing effect of the upper troposphere, so the overall outflow from the storms stays about the same. Our study aligns with the main idea of the FAT hypothesis, which postulates that in a warming climate, the temperature of the anvils (i.e., wide, flat clouds crawling out of the storm top) stays relatively constant primarily due to a thermodynamic constraint. However, our results show that convective-scale processes with dynamic control play a key role as well, providing an update to the FAT as originally proposed.

1. Introduction

One of the primary effects of tropical deep convection on climate arises through cirrus anvils developed from deep convective outflows. These cirrus anvils cause a considerable radiative warming in the upper troposphere (UT) and play an important role in radiative-convective feedbacks (e.g., Stephens, Van Den Heever, & Pakula, 2008). Therefore, knowing where and how convective outflows occur in relation to the environment is vital for understanding the present and future climate.

The source of convective outflows is vertically transported mass by convective updrafts that is eventually exported horizontally. For vertical transport, the primary center of action is the convective core, and one of the key processes that affects the convective core is entrainment. Entrainment dilutes the strength of convective updraft cores and reduces convective buoyancy, which in turn weakens the intensity of vertical transport and lowers the convective outflow levels (Houze, 2014). It has been believed that the effect of entrainment dilution is smaller for larger convective cores (i.e., the larger the core, the smaller the entrainment rate) since they are better protected from the environment and thus are less diluted by entrainment (e.g., Simpson & Wiggert, 1969). Thus,

Writing – original draft: Hanii Takahashi, Zhengzhao Johnny Luo, Hirohiko Masunaga, Akira T. Noda
Writing – review & editing: Hanii Takahashi, Zhengzhao Johnny Luo, Hirohiko Masunaga, Rachel Storer, Akira T. Noda

entrainment rate, convective core characteristics, and the relationship between them is among the crucial subjects to explore.

CloudSat Cloud Profiling Radar (CPR) can reveal the internal vertical structure of deep convection including both embedded convective cores and attached anvil outflows. The anvil outflows are tightly linked conceptually to the level of neutral buoyancy (LNB), where convection stops ascending and starts to detrain convective mass horizontally. Based on CloudSat CPR, a series of our previous works (Takahashi et al., 2017, 2021, 2023; Takahashi & Luo, 2012, 2014) have developed methods to estimate the intensity of convective cores, the degree of entrainment dilution, and convective outflow levels, including the maximum convective detrainment levels, through the concept of LNB. These studies also examined the entrainment-core relation on the basis of derived convective properties.

Our recent studies (Takahashi et al., 2017, 2021) have suggested that compared to oceanic deep convection, continental deep convection tends to have less diluted and wider convective cores that are associated with stronger convective updrafts and higher convective outflows. Interestingly, our result indicates a negative correlation between convective entrainment rate (λ) and size of the convective core (R). This inverse λ-R relation has been adopted as an important assumption in cumulus cloud modeling since the 1960s (e.g., Simpson & Wiggert, 1969): Simpson et al. (1965) formulated it as $\lambda = \frac{1}{M}\frac{dM}{dz} = \frac{9}{32}\frac{K}{R}$, where M is the mass in the rising convective tower and K is the entrainment coefficient. Based on the laboratory results (Turner, 1962, 1963), K was estimated to be 0.71, which led to the well-known equation of $\lambda = \frac{\alpha}{R}$ with $\alpha = 0.2$. However, the inverse λ-R relation had never been systematically explored based on satellite observations. Takahashi et al. (2021) is the first, to our knowledge, to support the inverse correlation based on CloudSat observations, to show that the inverse λ-R relation cannot simply scale with a fixed value of α, and to confirm that convective cores are wider and entrainment rates are larger over land than ocean, mainly due to deeper planetary boundary layers over land than ocean (Takahashi et al., 2023).

In this study, we expand our analysis to investigate the inverse λ-R relation focusing on the El Niño/La Niña contrast. It is known that caution needs to be taken when we interpret an El Niño/La Niña comparison in reference to long-term climate change. Nevertheless, studying interannual variations will provide unique insights into how convection may change in a warmer climate. Deepening our knowledge of where convective outflows occur and how they vary under natural climate variability has important implications for better understanding current and future climate.

Hartmann and Larson (2002) addressed these aspects, proposing a hypothesis that the temperature at the convective outflow level is not sensitive to the surface temperature and will stay mostly constant during climate changes. This is known as the fixed anvil temperature (FAT) hypothesis. The FAT hypothesis can be explained by a simple argument based on a consideration of the large-scale energy and mass balance. This is because the convective outflow is related to clear-sky subsidence (conservation of mass) that is controlled by clear-sky radiative cooling rate (energy balance), and also because the clear-sky radiative cooling rate depends primarily on water vapor and hence is a strong function of temperature (the Clausius–Clapeyron relation). Therefore, one should expect the convective outflow level to be concentrated at the temperature where water vapor concentrations and the associated radiative cooling decrease rapidly with height. It follows that temperature of the maximum convective outflow should remain largely unchanged as climate warms. The FAT hypothesis was later slightly modified by Zelinka and Hartmann (2010) as the Proportionately Higher Anvil Temperature (PHAT), which took into account a slight change of static stability, but the general idea remains similar.

The FAT and PHAT hypotheses have been supported by cloud-resolving model simulations (e.g., Kuang & Hartmann, 2007) and evaluated by observations in the context of El Niño-Southern Oscillation (ENSO) time scales (Li et al., 2012; Xu et al., 2007; Zelinka & Hartmann, 2011). Xu et al. (2007) showed that the FAT hypothesis is generally valid for cloud top temperature (CTT) with horizontally large clouds (e.g., diameters greater than 300 km) using the Tropical Rainfall Measuring Mission (TRMM)/Clouds and the Earth's Radiation Energy System (CERES) Single Scanner Footprint data (Wielicki et al., 1996). Using A-Train observations (Stephens et al., 2002; L'Ecuyer & Jiang, 2010), Zelinka and Hartmann (2011) examined variability in tropical high clouds and demonstrated that the cloud top heights change approximately isothermally in accordance with the FAT/PHAT hypothesis and the changes can be well explained by upper-tropospheric convergence computed from the mass and energy budget of the clear sky. Similar findings were obtained in Li et al. (2012), although they pointed

out there are regional variations. One caveat in the above-mentioned observational studies is that they all focused on CTT, whereas the FAT hypothesis applies to the maximum mass outflow of tropical deep convection. Analysis of ground-based and airborne radar observations showed that the maximum mass outflow of deep convection is usually a few kilometers lower than the top of cirrus anvils (Mullendore et al., 2009; Takahashi et al., 2017; Takahashi & Luo, 2012). In this study, we also use observations from CloudSat CPR to examine the variation of deep convective outflow to further test the FAT hypothesis.

This is a follow on to a series of recent publications that exploits the CloudSat vertical profiling view of deep convection to elucidate the relationships between convective outflows and a number of factors that influence convective outflow levels, including characteristics of convection itself (e.g., entrainment-core relation) and thermodynamic structure of the atmosphere (e.g., LNB), as well as large-scale energy and mass balance (e.g., large-scale convergence/divergence, and the FAT or PHAT hypothesis). In this study, we cast these relationships into the context of natural climate variability by contrasting changes associated with different phases of the ENSO cycle. First, we investigate the variation of entrainment rate (λ) and the size convective cores (R) during El Niño and La Niña, to reveal if the inverse λ-R relation changes with the ENSO phases. This investigation shows what controls the amount of entrainment dilution and helps to deepen our understanding of convective outflow mechanisms. Second, we explore how the altitude and temperature at convective outflows change between El Niño and La Niña. We use ERA5 reanalysis to examine the ENSO variation of altitudes and temperatures where peak divergence occurs in order to discuss the results in light of the FAT/PHAT hypothesis. The rest of the paper is organized as follows. Section 2 describes the data and analysis methods used in this study. Results are presented in Section 3 and Section 4 summarizes and interprets the findings.

2. Data and Methodology

2.1. CloudSat Observations

CloudSat (http://cloudsat.cira.colostate.edu) is a polar-orbiting satellite having the equator crossing time of ∼1:30 a.m./p.m in local solar time. CloudSat carries a 94-GHz (Cloud Profiling Radar) CPR whose footprint is around 1.7 km along track and 1.3 km across track with the vertical resolution of 480 m (oversampled to 240 m). The CloudSat CPR is sensitive to both cloud-size and precipitation-size particles. Two CloudSat products, 2B-GEOPROF and ECMWF-AUX, are used in this study. The former provides radar reflectivity and cloud mask, and the latter provides temperature and moisture profiles from the European Center for Medium-Range Weather Forecast (ECMWF) operational analysis interpolated in space and time to the CloudSat track. Stephens, Vane, et al. (2008) summarizes an overview of the CloudSat mission.

2.2. AIRS Observations

In this study, we use the Atmospheric Infrared Sounder (AIRS) data to evaluate moist static energy (MSE) profiles in Sections 3.2 and 3.3. AIRS onboard the Aqua satellite employs a cross-track scanning sounder that utilizes infrared radiances to retrieve temperature and moisture profiles. At nadir, AIRS achieves a horizontal resolution of roughly 13.5 km. The accuracy of AIRS temperature measurements is approximately 1 K over non-polar ocean surfaces from the surface up to 300 hPa, as well as over land from 2 km to 300 hPa. Furthermore, the accuracy ranges from 1 to 2 K over non-polar land surfaces from the surface to 2 km and in polar regions (Tian et al., 2013). Across the tropics, AIRS temperature sampling biases span from −1.5 to 0.75 K at 850 hPa and ±0.25 K at 500 and 300 hPa (as depicted in Figure 2 and Figure S1 in Hearty et al., 2014). A comprehensive analysis of the AIRS data is available in Chahine et al. (2006).

2.3. ERA5 Reanalysis

The ECMWF Reanalysis version 5 (ERA5) provides hourly, quarter-degree gridded data of atmospheric variables (Hersbach et al., 2020). The ERA5 horizontal winds matched in space and time to the CloudSat tracks are employed to calculate the vertical profile of horizontal divergence from 1,000 hPa to 50 hPa. Similar to Ito and Masunaga (2022), the divergence profiles averaged over a rain-free area within ±5° around the center of convective cores are estimated for each selected anvil cloud object described next.

2.4. Selection of Anvil Cloud Objects, Convective Core, and Convective Outflows

Since El Niño warming is generally maximized in boreal winter, we focus our analysis on December, January and February (DJF). Based on the Niño 3.4 index (5°N–5°S, 120°W–170°W), we select El Niño (2006–2007DJF, 2009–2010DJF) and La Niña (2007–2008DJF, 2010–2011DJF) months over the whole tropics (30°N–30°S). A total of 595 and 486 single-core anvil cloud objects are selected during El Niño and La Niña, respectively, over the whole tropics based on 5 years (2006–2011) of CloudSat data similarly to Takahashi et al. (2017, 2021, 2023). As in these previous studies, we focus on the single-core cases in our analysis to facilitate a straightforward interpretation of the relationship between convective core properties and the ambient clear-sky environment.

The selection method of convective cores and convective outflows is as follows. First, we define deep convective cloud objects based on 2B-GEOPROF data when cloud mask ≥20 (, which corresponds to reflectivity - 30 dBZ) and there is a continuous CPR echo from cloud top (≥10 km) to within 2 km above the surface. When an area of echo top height (ETH) of 10 dBZ ≥10 km is observed in a deep convective cloud, which is our definition of deep convective cores (DCCs), then we search on both sides of the cloud object for attached anvils. Note that ETH of 10 dBZ is the highest altitude that a 10 dBZ radar echo reaches, and thus the radius (R) of DCCs is defined as $\frac{size\ of\ DCC}{2}$. Anvils should have a cloud mask ≥20 and cloud base ≥5 km, and the horizontal extension of the anvil should be ≥20 km to ensure that the anvil is well developed. Deep convective cloud objects with convective cores and these attached anvils are called anvil cloud objects.

These well-developed anvil outflows are tightly linked to the concept of level of neutral buoyancy calculated using the ambient sounding (LNB_{sounding}), where convection stops ascending and starts to detrain mass horizontally. For each selected anvil cloud object, we estimate two forms of convective outflow levels based on satellite observations, or $LNB_{\text{observation}}$: LNB_{CTH} and $LNB_{maxMass}$. These terms follow the terminology of Takahashi and Luo (2012) as well as Takahashi et al. (2017, 2021, 2023). A schematic showing LNB_{sounding}, LNB_{CTH} and $LNB_{maxMass}$ can be found in Takahashi et al. (2017, Figure 1). LNB_{CTH} is the cloud top height (CTH) of the anvils and represents the highest detrainment level. $LNB_{maxMass}$ is the height where the maximum radar reflectivity within the anvil column is observed, and is most relevant to convective mass transport since it has been well correlated with the maximum mass detrainment level (Mullendore et al., 2009). Note that LNB_{CTH} and $LNB_{maxMass}$ are calculated profile by profile first and then averaged only over the "fresh" anvils. Here "fresh" anvils refer to the anvil clouds within the first 20 km in distance from the convective core. This approach is taken to reduce the impact of bias caused by particle sedimentation, which tends to prolong the anvil lifetime beyond the control of parent convective core.

2.5. Measurement of Entrainment Dilution

LNB_{sounding} is estimated based on a parcel theory valid for the ideal case of an undiluted convective core in the absence of entrainment. However, in reality, convection interacts with the environment and loses buoyancy due to entrainment dilution, which is the case of $LNB_{\text{observation}}$. Therefore, as Takahashi et al. (2017) suggested, the difference between LNB_{sounding} and $LNB_{\text{observation}}$ can be interpreted as a measure of the magnitude of the entrainment effects: the greater the entrainment dilution, the larger the height difference. We estimate LNB_{sounding} based on the moist static energy ($MSE = C_pT + gz + L_vq$, where C_p, g, z, L_v, and q are the specific heat of condensation, the gravitational constant, height, the latent heat of vapourization, and specific humidity, respectively) using temperature and moisture profiles from ECMWF operational analysis interpolated in space and time to the CloudSat track. LNB_{sounding} is the level where MSE is equal to the maximum MSE between the surface and 925 hPa (Liu & Zipser, 2005).

The difference between LNB_{sounding} and $LNB_{\text{observation}}$ can be cast into a simple framework of a one-dimensional entraining plume model:

$$\frac{\partial MSE_p}{\partial z} = \lambda(MSE_e - MSE_p), \tag{1}$$

where subscripts p and e refer to properties of the in-cloud air parcel and of the environment, respectively. Following a similar approach to Luo et al. (2010), we calculate the moist static energy (MSE) of an air parcel for various values of λ. To do this, we integrate Equation 1 over height using collocated ECMWF profiles of temperature and humidity from the planetary boundary layer (PBL). The ECMWF sounding represents the ambient

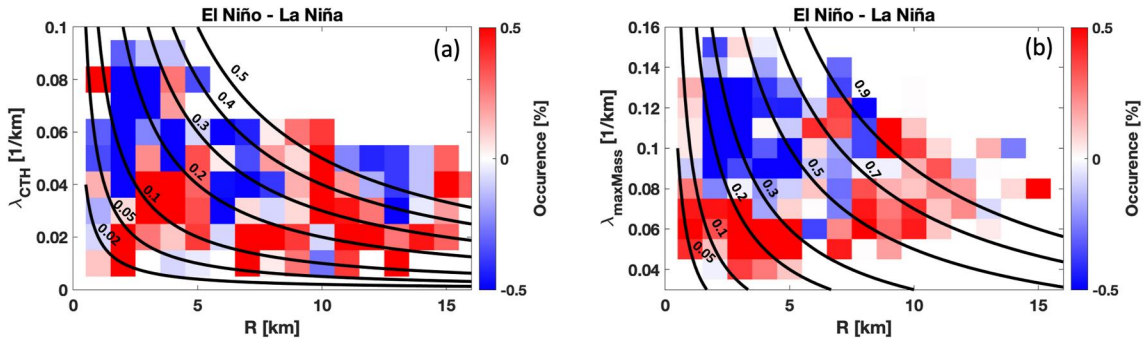

Figure 1. The difference between convective cloud objects over El Niño and La Niña, as a function of convective core radius size (x axis) and entrainment rate relative to (a) LNB_{CTH} or (b) $LNB_{maxMass}$ (y axis). The black contour lines show values of (a) α_{CTH} or (b) $\alpha_{maxMass}$.

environment surrounding the air parcel. We start with λ set at 1% per kilometer and increase it by an increment of 1% per kilometer at each step. The iterative process continues until we find a value of λ that satisfies the condition of neutral buoyancy for the air parcel at the specified outflow level (the calculated MSE_p is almost equal to the saturated MSE at LNB). In this way, we can estimate bulk entrainment rates, λ_{CTH} and $\lambda_{maxMass}$ (unit: %/km) relative to LNB_{CTH} and $LNB_{maxMass}$, respectively. Detailed information of selection of convective cloud objects, estimation of LNB_{CTH} and $LNB_{maxMass}$ as well as λ_{CTH} and $\lambda_{maxMass}$ can be found Takahashi and Luo (2012) and Takahashi et al. (2017, 2021, 2023).

3. Result

3.1. The Entrainment-Core Relation

The differences between El Niño and La Niña in the joint probability distribution of λ and R are shown in Figure 1, with black contour lines of α (i.e., $\lambda = \frac{\alpha}{R}$) with respect to LNB_{CTH} and $LNB_{maxMass}$ following Takahashi

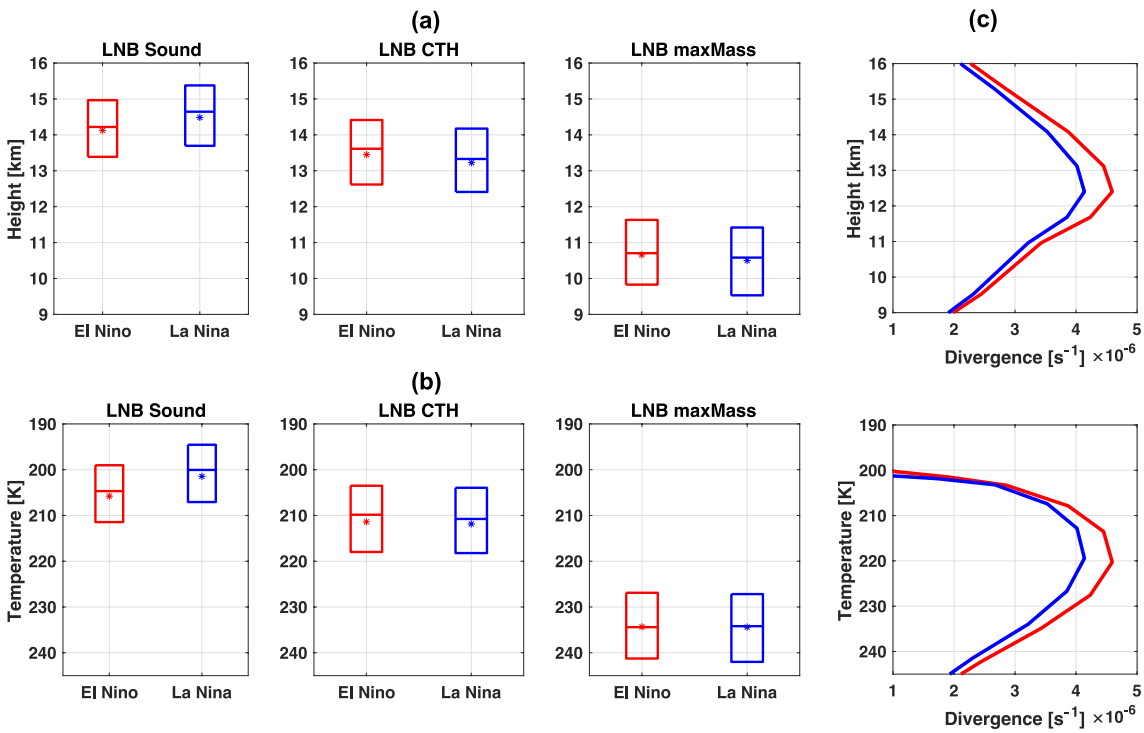

Figure 2. Box-scatter diagrams for (a) altitudes (top panels) and (b) temperature (bottom panels) of $LNB_{sounding}$ and $LNB_{observation}$ (LNB_{CTH} and $LNB_{maxMass}$) during El Niño (red) and La Niña (blue) whose bottom and top of the boxes show, respectively, the 25 and 75 percentiles, the stars show the mean, and the central lines show the median, together with (c) the divergence profiles during El Niño (red) and La Niña (blue).

et al. (2021). Results clearly show that convection in El Niño and La Niña events are clustered into different domains in the λ-R space, and together they accentuate the inverse λ-R relationship. Convective clouds during El Niño tend to have smaller λ and larger R compared to La Niña, which seems to suggest that convective cores are more intense and better protected during El Niño than La Niña. This implies that vertical mass transport by convective cores is more efficient (i.e., not as much diluted by the ambient air mass) during El Niño than La Niña.

3.2. Variation of Convective Outflows

LNB_{sounding} and $LNB_{\text{observation}}$, the latter of which is represented by LNB_{CTH} and $LNB_{maxMass}$ collectively, are compared between El Niño (red) and La Niña (blue) in terms of altitude in Figure 2a (top panels) and temperature in Figure 2b (bottom panels). It is interesting that LNB_{sounding} is higher during La Niña than in El Niño, while the opposite is true for $LNB_{\text{observation}}$. In terms of median, LNB_{sounding} during La Niña is 0.43 km higher than that during El Niño, whereas LNB_{CTH} and $LNB_{maxMass}$ during El Niño are 0.28 and 0.12 km higher than those during La Niña, respectively. The Student's *t-test* confirms that the differences in LNB_{sounding} and LNB_{CTH} are statistically significant at the 0.95 confidence level, while there are little differences in $LNB_{maxMass}$.

To test the FAT or PHAT hypothesis, temperatures at LNB_{sounding} and $LNB_{\text{observation}}$ are examined in Figure 2b (bottom panels). LNB_{sounding} has a significant temperature difference between El Niño and La Niña: the median value of LNB_{sounding} is 4.63 K warmer during El Niño than during La Niña. However, the temperature difference between El Niño and La Niña is very small in $LNB_{\text{observation}}$, especially for $LNB_{maxMass}$: the differences in median values for LNB_{CTH} and $LNB_{maxMass}$ are 0.92 and 0.21 K, respectively.

If one converts height differences (0.28 km for LNB_{CTH} and 0.12 km for $LNB_{maxMass}$) to temperatures assuming a moist adiabatic lapse rate (which is close to 9.8 K/km at 12 km where water vapor is scarce), then the temperature difference for LNB_{CTH} and $LNB_{maxMass}$ would be 2.8 and 1.2 K, respectively. However, the actual temperature differences for these levels are only 0.92 and 0.21 K, respectively. The Student's *t-test* also indicates that the temperature difference in LNB_{sounding} is statistically significant at the 0.95 confidence level, but that is not significant in $LNB_{\text{observation}}$. Hence, the temperature at the convective outflow levels (LNB_{CTH} and $LNB_{maxMass}$) is even less variable across different phases of the ENSO cycle than expected from the small difference in altitude. This seems to echo the FAT/PHAT hypothesis, although the ENSO cycle is not a surrogate for climate change. The most intriguing part is that the FAT hypothesis is more evident when looking at $LNB_{maxMass}$ (i.e., the smallest temperature difference) than at LNB_{CTH}; this is consistent with the idea that $LNB_{maxMass}$ is most relevant to convective mass outflow and convective transport.

Originally, the FAT/PHAT hypotheses were built upon the assumption that the anvil height is predominantly determined by temperature through divergence directly below the tropical tropopause layer. However, how the dynamical field (divergence) strongly constrains the anvil height has not been verified at a process level. Therefore, it is of great interest to explicitly examine the relationship between $LNB_{\text{observation}}$ and the height where maximum wind divergence occurs. Figure 2c summarizes the wind divergence profiles during El Niño and La Niña, which shows that the peak of divergence occurs around 12.5 km and 220 K across the ENSO phases. Interestingly, the peak of wind divergence occurs in between LNB_{CTH} and $LNB_{maxMass}$. Since the FAT hypothesis assumes that the maximum divergence determines the height of convective detrainment, it makes sense that the height of $LNB_{\text{observation}}$ and the height of maximum wind divergence are closely related, and their variations are also similar. Our results confirm that the difference in height between $LNB_{\text{observation}}$ and maximum wind divergence remains relatively constant across the ENSO phases.

LNB_{sounding}, on the other hand, shows a different behavior compared to $\text{LNB}_{\text{observation}}$. To understand why LNB_{sounding} is higher during La Niña than El Niño, Figure 3a shows MSE (solid line) and MSE^* (saturated moist static energy, dotted line) during El Niño (red line) and La Niña (blue line) over the anvil cloud objects. The vertical arrows demonstrate the corresponding pseudoadiabatic pathways based on parcel theory. As expected, MSE is higher during El Niño than La Niña at all levels. The difference is smaller near the surface (the difference is ∼716 J/kg at 0.2 km) than in the upper troposphere or UT (the difference is ∼1,215 J/kg at 12 km). In the warmer ENSO phase, the MSE in the upper troposphere changes more rapidly with height than MSE in the lower troposphere, such that the MSE curve in the UT is more "squashed" during El Niño than in La Niña. This leads to an LNB_{sounding} that is higher during La Niña than during El Niño. So why is the MSE difference near the surface small and the MSE difference in the UT large?

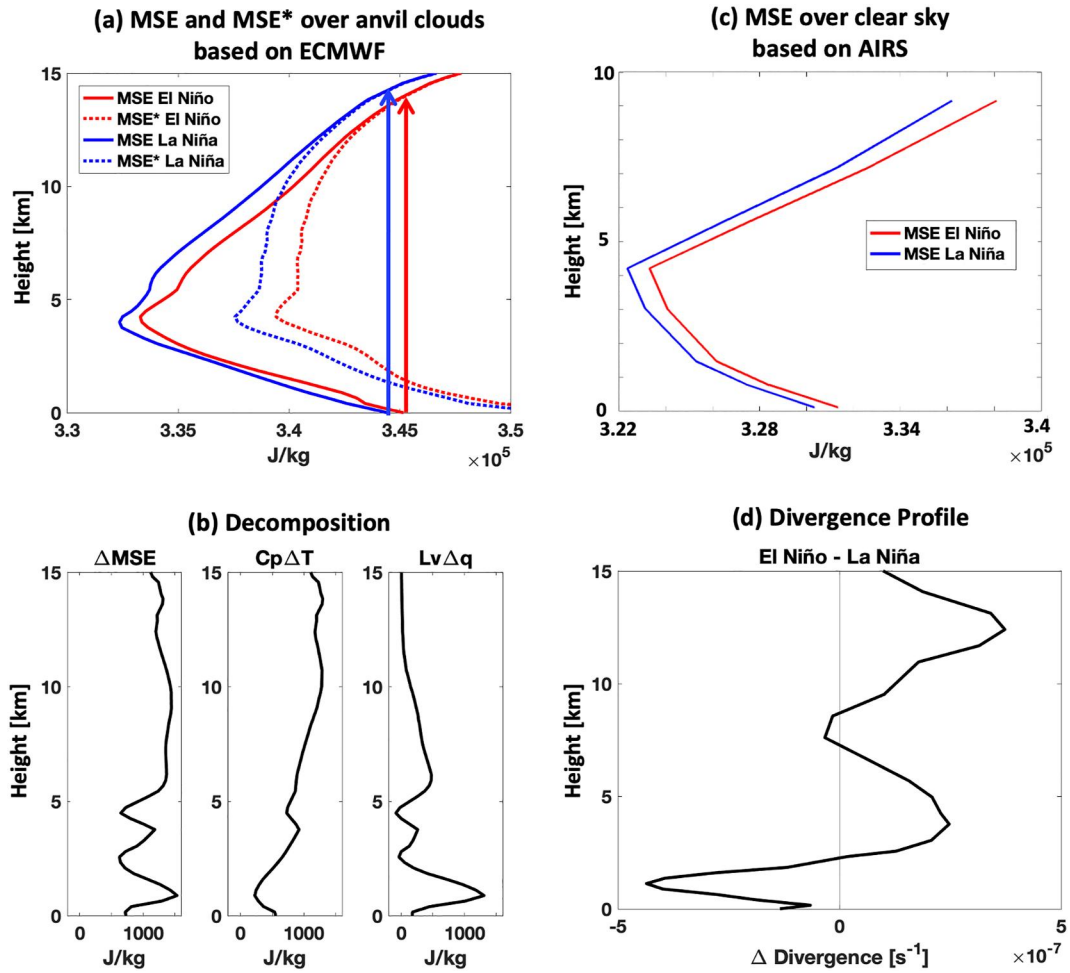

Figure 3. (a) MSE (solid line) and MSE* (dotted line) during El Niño (red line) and La Niña (blue line), together with the thermodynamic pathways based on parcel theory during El Niño (red arrow) and La Niña (blue arrow) based on ECMWF-AUX. (b) The illustration of relative importance of ΔMSE due to the temperature change (ΔT) and due to the specific humidity change (Δq) based on ECMWF-AUX. (c) MSE over the whole tropics during El Niño (red line) and La Niña (blue line) based on AIRS. (d) The divergence changes during El Niño and La Niña based on ERA5.

3.3. A Synthesis

To answer this question, we decompose the change of *MSE* (i.e., *MSE* difference between El Niño and La Niña) over the anvil cloud objects into two terms, the change of temperature (T) and the change of specific humidity (q):

$$\Delta MSE = C_p \Delta T + L_v \Delta q,$$

where

$$\Delta MSE = MSE_{EL} - MSE_{LA},$$

$$\Delta T = T_{EL} - T_{LA},$$

$$\Delta q = q_{EL} - q_{LA},$$

and the notation of *EL* and *LA* refer to the El Niño and La Niña, respectively. To understand what controls the *MSE* change ($\Delta MSE = MSE_{EL} - MSE_{LA}$), Figure 3b illustrates the relative contribution of ΔMSE due to the temperature change (ΔT) and due to the specific humidity change (Δq). It shows that ΔMSE near the surface and

near the UT are mostly controlled by Δq *and* ΔT, respectively. The fact that the temperature difference near the UT is larger than that near the surface leads to an enhanced stability in the UT during El Niño. This is a key cause for the difference in LNB_{sounding} between El Niño and La Niña.

We also examine *MSE* over the whole tropics during El Niño and La Niña, including non-cloudy regions, based on AIRS in Figure 3c. It is confirmed that even if we include non-cloudy regions, the tendency toward smaller ΔMSE near the surface and larger ΔMSE in the UT is observed. This UT stabilization effect supports the above conclusion from ERA-based MSE data. One consequence of the UT stabilization is that an undiluted air parcel ascending from the surface will lose buoyancy at a lower altitude. This effect alone should favor convective outflows at lower altitudes during El Niño.

Why, then, do convective outflows end up occurring at roughly the same level during El Niño and La Niña? Our analysis indicates that this is made possible by stronger convective intensity during El Niño than La Niña: the inverse λ-R relation (Section 3.1) illustrates that deep convection has a smaller entrainment effect and larger convective cores during El Niño than La Niña, both pointing to stronger convective intensity during El Niño than La Niña. Hence, although the environment is less favorable for convection to grow deeper during El Niño, stronger convective intensity compensates for the disadvantage, resulting in the same outflow levels as during La Niña. Moreover, as illustrated in Figure 3d, convergence is stronger in the lower levels and divergence is larger in the upper levels during El Niño compared to La Niña. This provides additional evidence for a stronger convective intensity during El Niño than during La Niña.

4. Summary and Interpretation

This study takes full advantage of CloudSat vertical profiling of deep convection to elucidate the relationships between convective outflow and important factors that affect it, including environmental factors (e.g., *LNB*, large-scale convergence/divergence, and the FAT or PHAT hypothesis), and convective cloud properties (e.g., entrainment dilution and convective cores). To achieve this, we analyze and compare convective outflows based on the parcel theory (LNB_{sounding}) and those based on the CloudSat observations ($LNB_{\text{observation}}$), along with investigating the relationship between entrainment and convective core, specifically during El Niño and La Niña events. Four key findings from this study are summarized as follows:

- The altitude of $LNB_{\text{observation}}$ experiences a slight elevation during El Niño, while the temperature at $LNB_{\text{observation}}$ remains insensitive to ENSO cycles, which is most evident for $LNB_{maxMass}$.
- $LNB_{\text{observation}}$ and the level corresponding to maximum wind divergence are closely related to each other, and their association remains constant across different phases of the ENSO cycle.
- Upper-tropospheric stabilization leads to a lower LNB_{sounding} during El Niño than La Niña.
- The contrast between El Niño and La Niña in the entrainment-core diagram suggests that convective cores are more intense and less diluted during El Niño than La Niña.

The first and second findings indicate that the altitudes of convective outflow levels undergo some changes across over different phases of the ENSO cycle, while the temperatures of these levels remain relatively constant. This is largely consistent with what the FAT hypothesis predicts, although the underlying mechanism differs from the original theory. Unlike previous studies that relied on cloud tops, our study uses convective outflow levels derived from CloudSat CPR profiles of cirrus anvils, providing a more direct observation of mass outflow. As a result, the FAT hypothesis is most evident in the results based on $LNB_{maxMass}$, which is most relevant to the maximum convective detrainment level.

The third finding reveals upper-tropospheric (UT) stabilization during El Niño compared to La Niña, which, on its own, would suppress the vertical development of deep convection, seemingly contradicting the first and second findings. The fourth finding provides a reconciliation, that is, convection becomes more intense during El Niño, offsetting the less favorable thermodynamic environment. Both smaller entrainment rate and larger convective core size during El Niño point to an increase in convective intensity. The reduced entrainment rate during the warm phase of the ENSO could be linked to a moister mid-troposphere that diminishes the impact of entrainment dilution, enabling deeper convection development (e.g., Henderson et al., 2018; Jensen & Del Genio, 2006). It's important to point out that while the original FAT hypothesis predicts a near-constant anvil temperature due to temperature control of radiative cooling (via the Clausius–Clapeyron relationship) and large-scale wind divergence, our study takes a step further. We identify detailed convective-scale processes and mechanisms that

contribute to achieving this outcome. This finding advances the FAT and PHAT hypotheses. An implication of the current findings is that the height of cirrus anvils is not always directly tied to the environmental sounding as originally assumed by the FAT theory (see Seeley et al., 2019 for another example).

Our results show that convective processes undergo changes during El Niño and La Niña, leading to nearly constant convective outflow levels. Although our analysis is based on a fixed sampling time (around 1:30 a.m./p.m. local time), potentially introducing certain biases, it contributes to advancing our knowledge of the relationships between convective outflows and influencing factors. This not only enhances understanding of the mechanisms responsible for convection-climate feedback, but also has the potential to improve the representation of convection in global models by incorporating the observed relationships into the parameterization schemes.

Finally, it is also worth mentioning uncertainties in R, λ, and $\mathrm{LNB}_{\mathrm{observation}}$ associated with our analysis, which are documented in Takahashi et al. (2021). The main sources of uncertainties in R derive from potential bias in sampling geometry since CloudSat CPR does not always profile through the center of the cores, and our estimation of R could be systematically underestimated by approximately 21%. Additionally, the variation of $LNB_{\mathrm{observation}}$ leads to ±2.00%/km uncertainties in λ. As these biases and uncertainties are consistent during ENSO cycles, we do not expect this issue to impact our comparison between El Niño and La Niña.

Data Availability Statement

The data of A-Train observations can be found from the CloudSat Data Processing Center at www.cloudsat.cira.colostate.edu. More specifically, detailed information on 2B-GEOPROF and ECMWF-AUX data can be found from the CloudSat Data Processing Center at https://www.cloudsat.cira.colostate.edu/data-products/2b-geoprof products/2b-geoprof, and https://www.cloudsat.cira.colostate.edu/data-products/ecmwf-aux, respectively. The instructions for how to access 2B-GEOPROF and ECMWF-AUX are summarized at https://www.cloudsat.cira.colostate.edu/order/sftp-access.

Acknowledgments
The research was carried out at the Jet Propulsion Laboratory, California Institute of Technology, under a contract with the National Aeronautics and Space Administration (NASA). This study was supported by NASA Grant 80NSSC20K0090 and part of this work was performed at the Jet Propulsion Laboratory, California Institute of Technology, under a contract with the National Aeronautics and Space Administration (80NM0018D0004, Project/Task is 105357/967701.02.01.03.05) as well as funding support from INCUS project under Grant 80LARC22DA011 (Project/Task is 107931/04.01.A01, and 108177/04.01.A01). ZJL would like to acknowledge funding support from NASA Grants 80NSSC18K1600 and 80NSSC23K0116 awarded to CUNY. ATN was supported by the Advanced Studies of Climate Change projection (SENTAN) JPMXD0722680395 from the Japanese Ministry of Education, Culture, Sports, Science and Technology.

References

Chahine, M. T., Pagano, T. S., Aumann, H. H., Atlas, R., Barnet, C., Blaisdell, J., et al. (2006). AIRS: Improving weather forecasting and providing new data on greenhouse gases. *Bulletin of the American Meteorological Society*, *87*(7), 911–926. https://doi.org/10.1175/bams-87-7-911

Hartmann, D. L., & Larson, K. (2002). An important constraint on tropical cloud-climate feedback. *Geophysical Research Letters*, *29*(20), 12-1–12-4. https://doi.org/10.1029/2002gl015835

Henderson, D. S., Kummerow, C. D., & Berg, W. (2018). ENSO influence on TRMM tropical oceanic precipitation characteristics and rain rates. *Journal of Climate*, *31*(10), 3979–3998. https://doi.org/10.1175/JCLI-D-17-0276.1

Hersbach, H., Bell, B., Berrisford, P., Hirahara, S., Horányi, A., Muñoz Sabater, J., et al. (2020). The ERA5 global reanalysis. *Quarterly Journal of the Royal Meteorological Society*, *146*(730), 1999–2049. https://doi.org/10.1002/qj.3803

Houze, R. A., Jr. (2014). *Cloud dynamics* (Vol. 104). Academic press.

Ito, M., & Masunaga, H. (2022). Process-level assessment of the iris effect over tropical oceans. *Geophysical Research Letters*, *49*(7), e2022GL097997. https://doi.org/10.1029/2022gl097997

Jensen, M. P., & Del Genio, A. D. (2006). Factors limiting convective cloud-top height at the ARM Nauru Island climate research facility. *Journal of Climate*, *19*(10), 2105–2117. https://doi.org/10.1175/jcli3722.1

Kuang, Z., & Hartmann, D. L. (2007). Testing the fixed anvil temperature hypothesis in a cloud-resolving model. *Journal of Climate*, *20*(10), 2051–2057. https://doi.org/10.1175/jcli4124.1

L'Ecuyer, T. S., & Jiang, J. H. (2010). Touring the atmosphere aboard the A-Train. *Physics Today*, *63*(7), 36–41. https://doi.org/10.1063/1.3463626

Li, Y., Yang, P., North, G. R., & Dessler, A. (2012). Test of the fixed anvil temperature hypothesis. *Journal of the Atmospheric Sciences*, *69*(7), 2317–2328. https://doi.org/10.1175/jas-d-11-0158.1

Liu, C., & Zipser, E. J. (2005). Global distribution of convection penetrating the tropical tropopause. *Journal of Geophysical Research*, *110*(D23). https://doi.org/10.1029/2005jd006063

Luo, Z. J., Liu, G. Y., & Stephens, G. L. (2010). Use of A-Train data to estimate convective buoyancy and entrainment rate. *Geophysical Research Letters*, *37*(9). https://doi.org/10.1029/2010gl042904

Mullendore, G. L., Homann, A. J., Bevers, K., & Schumacher, C. (2009). Radar reflectivity as a proxy for convective mass transport. *Journal of Geophysical Research*, *114*(D16). https://doi.org/10.1029/2008jd011431

Seeley, J. T., Jeevanjee, N., & Romps, D. M. (2019). FAT or FiTT: Are anvil clouds or the tropopause temperature invariant? *Geophysical Research Letters*, *46*(3), 1842–1850. https://doi.org/10.1029/2018gl080096

Simpson, J., Simpson, R. H., Andrews, D. A., & Eaton, M. A. (1965). Experimental cumulus dynamics. *Reviews of Geophysics*, *3*(3), 387–431. https://doi.org/10.1029/rg003i003p00387

Simpson, J., & Wiggert, V. (1969). Models of precipitating cumulus towers. *Monthly Weather Review*, *97*(7), 471–489. https://doi.org/10.1175/1520-0493(1969)097<0471:mopct>2.3.co;2

Stephens, G. L., Van Den Heever, S., & Pakula, L. (2008). Radiative–convective feedbacks in idealized states of radiative–convective equilibrium. *Journal of the Atmospheric Sciences*, *65*(12), 3899–3916. https://doi.org/10.1175/2008jas2524.1

Stephens, G. L., Vane, D. G., Boain, R. J., Mace, G. G., Sassen, K., Wang, Z., et al. (2002). The CloudSat mission and the A-Train: A new dimension of space-based observations of clouds and precipitation. *Bulletin of the American Meteorological Society*, *83*(12), 1771–1790. https://doi.org/10.1175/bams-83-12-1771

Stephens, G. L., Vane, D. G., Tanelli, S., Im, E., Durden, S., Rokey, M., et al. (2008b). CloudSat mission: Performance and early science after the first year of operation. *Journal of Geophysical Research: Atmospheres*, *113*(D8). https://doi.org/10.1029/2008jd009982

Takahashi, H., & Luo, Z. (2012). Where is the level of neutral buoyancy for deep convection? *Geophysical Research Letters*, *39*(15). https://doi.org/10.1029/2012gl052638

Takahashi, H., & Luo, Z. J. (2014). Characterizing tropical overshooting deep convection from joint analysis of CloudSat and geostationary satellite observations. *Journal of Geophysical Research: Atmospheres*, *119*(1), 112–121. https://doi.org/10.1002/2013jd020972

Takahashi, H., Luo, Z. J., & Stephens, G. (2021). Revisiting the entrainment relationship of convective plumes: A perspective from global observations. *Geophysical Research Letters*, *48*(6), e2020GL092349. https://doi.org/10.1029/2020GL092349

Takahashi, H., Luo, Z. J., Stephens, G., & Mulholland, J. P. (2023). Revisiting the land-ocean contrasts in deep convective cloud intensity using global satellite observations. *Geophysical Research Letters*, *50*(5), e2022GL102089. https://doi.org/10.1029/2022GL102089

Takahashi, H., Luo, Z. J., & Stephens, G. L. (2017). Level of neutral buoyancy, deep convective outflow, and convective core: New perspectives based on 5 years of CloudSat data. *Journal of Geophysical Research: Atmospheres*, *122*(5), 2958–2969. https://doi.org/10.1002/2016jd025969

Tian, B., Fetzer, E. J., Kahn, B. H., Teixeira, J., Manning, E., & Hearty, T. (2013). Evaluating CMIP5 models using AIRS tropospheric air temperature and specific humidity climatology. *Journal of Geophysical Research: Atmospheres*, *118*(1), 114–134. https://doi.org/10.1029/2012jd018607

Wielicki, B. A., Barkstrom, B. R., Harrison, E. F., Lee, R. B., III, Smith, G. L., & Cooper, J. E. (1996). Clouds and the Earth's Radiant Energy System (CERES): An earth observing system experiment. *Bulletin of the American Meteorological Society*, *77*(5), 853–868. https://doi.org/10.1175/1520-0477(1996)077<0853:catere>2.0.co;2

Xu, K. M., Wong, T., Wielicki, B. A., Parker, L., Lin, B., Eitzen, Z. A., & Branson, M. (2007). Statistical analyses of satellite cloud object data from CERES. Part II: Tropical convective cloud objects during 1998 El Niño and evidence for supporting the fixed anvil temperature hypothesis. *Journal of Climate*, *20*(5), 819–842. https://doi.org/10.1175/jcli4069.1

Zelinka, M. D., & Hartmann, D. L. (2010). Why is longwave cloud feedback positive? *Journal of Geophysical Research: Atmospheres*, *115*(D16). https://doi.org/10.1029/2010jd013817

Zelinka, M. D., & Hartmann, D. L. (2011). The observed sensitivity of high clouds to mean surface temperature anomalies in the tropics. *Journal of Geophysical Research: Atmospheres*, *116*(D23). https://doi.org/10.1029/2011jd016459